

Formation of Willemite in Hydrothermal Environments

JOËL BRUGGER,[†]

*Department of Geology and Geophysics, University of Adelaide, 5000 South Australia,
and South Australian Museum, Adelaide, 5000 South Australia, Australia*

D. C. MCPHAIL,

*School of Geosciences, Monash University, Victoria 3800, Australia,
and Cooperative Research Centre for Landscape Environments and Mineral Exploration & Department of Geology,
The Australian National University, Canberra, ACT 0200, Australia*

MALCOLM WALLACE,

School of Earth Sciences, University of Melbourne, Victoria 3010, Australia

AND JOHN WATERS

School of Geosciences, Monash University, Victoria 3800, Australia

Abstract

Willemite (zinc silicate) is the main zinc mineral in some carbonate-hosted ore deposits (e.g., Franklin, New Jersey; Vazante, Brazil; Beltana, South Australia; Kabwe, Zambia). Recent interest in these unconventional zinc deposits has increased because of high zinc grades that exceed 40 wt percent, relatively low environmental impact of ore processing owing to the lack of acid-generating sulfides in the waste, and advances in ore processing technologies. In the past, most metallogenic studies proposed formation of willemite deposits by supergene or hypogene alteration of preexisting sulfide deposits. However, recent data on the Vazante, Beltana, and Kabwe deposits indicate willemite crystallization at temperatures in excess of 150°C, raising the possibility of primary precipitation from hydrothermal fluids.

We use numerical geochemical modeling to examine the formation of willemite under hydrothermal conditions. Activity-activity diagrams reveal that, in the presence of dissolved sulfur and quartz, willemite instead of sphalerite will precipitate under oxidizing (e.g., hematite-stable, sulfate-predominant) and alkaline (pH higher than K feldspar-muscovite-quartz) conditions. Willemite also becomes more stable, relative to sphalerite, at high temperature, and willemite can coexist with magnetite at 300°C. The stabilities and solubilities of sphalerite, willemite, smithsonite, hydrozincite, and zincite were calculated for wide ranges of temperature (25°–300°C), chloride concentration, dissolved sulfur and carbon concentrations, pH, quartz saturation, and oxidation potential. Plots of the solubility of the different minerals as a function of two variables (e.g., temperature and redox state; pH and redox state) allow us to predict the effects of changing chemical conditions, which in turn permits an estimate of the efficiency of particular precipitation processes. Cooling is an effective process for precipitating sphalerite but not willemite, whereas pH increase (e.g., by acidic fluids reacting with carbonates) is effective for precipitating willemite but not sphalerite.

Dynamic geochemical models that simulate physicochemical processes are used to understand the formation of the Beltana willemite deposit in the Adelaide geosyncline of South Australia. This small, high grade deposit (850,000 t at 36% Zn) is hosted in dolomite of the Cambrian Ajax Limestone, next to a tectonic contact with the diapiric, halite-bearing clastic sediments of the Callanna Group. The orebody is associated with hematite alteration and is characterized by the total absence of sulfides; willemite is the only zinc ore mineral, and the arsenate hedyphane ($\text{Ca}_2\text{Pb}_3[\text{AsO}_4]_3\text{Cl}$) is the main lead mineral. The model results show that willemite will precipitate in response to water-rock interaction and fluid mixing processes at temperatures above 120°C. The presence of arsenate in the hydrothermal fluid is likely to have been important at Beltana; in arsenate-absent models sulfate is reduced to sulfide by the precipitation of ferrous iron as hematite, resulting in the precipitation of sphalerite and galena. In contrast, in models including arsenate the reduction of sulfate to sulfide is inhibited and willemite is predicted to precipitate.

Introduction

WILLEMITE, Zn_2SiO_4 , is found in a wide variety of geological environments. It is a common accessory mineral formed during the low-temperature alteration of zinc-sulfide ores in arid environments, e.g., the Goodsprings district in Nevada (Takahashi, 1960) and Broken Hill in Rhodesia (Bariand et al., 1977), but it also may be associated with magmatic-hydrothermal

processes related to highly evolved alkaline magmas such as in south Greenland (Finch, 1990). Economic willemite-bearing deposits are attractive for several reasons: they have high zinc grades and less environmental impact than sulfide ore (e.g., no sulfur emissions or waste, little or no acid drainage), and the oxide ore can be used to improve the smelting of sulfide-rich Pb and Zn ore.

Economic willemite deposits show a large diversity of mineralization styles; however, known willemite occurrences that

[†] Corresponding author: e-mail, Joel.Brugger@adelaide.edu.au

possess ore grades and tonnage are restricted to carbonate host rocks. The most famous willemite deposits are probably the Sterling Hill (24 Mt at 19.6% Zn) and Franklin Furnace deposits in New Jersey (e.g., Frondel and Baum, 1974; Johnson et al., 1990). These deposits have undergone granulite-facies metamorphism, and hence the nature of the primary mineralization is difficult to decipher. The most recent of these studies favors a syngenetic exhalative or shallow hydrothermal origin for the highly oxidized orebody rather than metasomatism or alteration of a preexisting sulfide orebody (Johnson et al., 1990). The Vazante deposit in Minas Gerais, Brazil (19.2 Mt at 21 wt % Zn) is hosted in a shear zone and has been tectonically imbricated with small sulfide lenses (Monteiro et al., 1999). Recent isotopic and petrographic studies indicate formation temperatures between 206°C and 294°C, similar to the metamorphic temperatures. Consequently, Monteiro et al. (1999) advocated syndeformation precipitation of willemite. Willemite is a common mineral in the Otavi Mountain Cu-Pb-Zn-V-Ag-Ge-Ga province in Namibia (Piranjo and Joubert, 1993; Cairncross, 1997). The largest willemite deposit in this region is Berg Aukas, where karst-hosted Pb-Zn-Ag sulfide ore has been deeply weathered, and willemite is the main Zn mineral in the ore in large portions of the mine. The last stage of the alteration introduced large amounts of vanadium, interpreted to have been carried in oxidized fluids (Cairncross, 1997). A similar situation occurs at the Star Zinc deposit, one of the largest willemite resources in the Zambian copper belt (98,000 t Zn, unknown grade; Sweeney et al., 1991), where willemite also replaces sphalerite ores. Fluid inclusions in willemite from this deposit display large ranges in salinity (5–22 wt % NaCl equiv) and temperature (150–250°C; Sweeney et al., 1991), indicating that willemite replaced sphalerite under hydrothermal conditions. Finally, small high-grade willemite orebodies occur in Lower Cambrian carbonates of the Adelaide geosyncline in South Australia. These deposits have traditionally been interpreted as resulting from the alteration of preexisting sulfide orebodies (e.g., Horn, 1975), despite the lack of relict sulfide or replacement textures. Recent studies indicate that ore deposition took place at temperatures higher than 100°C (Burdett, 2000; Hallam, 2000) and suggest a primary hydrothermal origin for these deposits.

From this short review, it is clear that willemite can form under a wide variety of conditions in a variety of geologic environments from low to high temperature. Understanding the conditions of formation, especially in hydrothermal environments, has important implications for mineral exploration. In the case of low-temperature alteration, exploring for a willemite deposit is similar to exploring for a near-surface sulfide orebody. In the case of hydrothermal formation, however, exploration strategies need to be developed with an understanding of the nature of hydrothermal fluids and depositional processes. Hence, exploration may need to be targeted outside the zones favorable for sulfide orebodies.

The principal aim of this study is to examine the physical and chemical controls on the formation of willemite under hydrothermal conditions, using thermodynamic modeling. More specific aims are to assess the quality of available thermodynamic properties of zinc minerals and aqueous species, identify potential indicator minerals useful in exploring for

willemite-bearing hydrothermal deposits, and understand the physicochemical processes that are most important in forming at least some willemite-bearing hydrothermal deposits. We address the first several aims for the general case and the last using the example of the Beltana deposit in South Australia.

Hydrothermal Geochemistry of Zinc and Solubility of Willemite and Related Minerals

The solubilities of willemite and related minerals depend on several physical and chemical variables, such as pressure, temperature, acidity, redox state, ligand (e.g., chloride, sulfide, sulfate) concentrations, dissolved concentrations of other elements or compounds present in ore-bearing minerals (e.g., SiO₂ for willemite, CO₃²⁻ for smithsonite), and partial pressures of gases (e.g., CO₂, H₂S, H₂). In hydrothermal environments these variables can change in response to a variety of processes that include cooling, compression or decompression, fluid mixing, water-rock interaction, fluid immiscibility, and boiling. One or more of these processes may be important in the formation of willemite deposits under hydrothermal conditions. Understanding the conditions of willemite formation, especially relative to sphalerite and other zinc minerals, is a first step in understanding the processes.

We use numerical models to predict the aqueous speciation of zinc and solubilities of zinc and other minerals over wide ranges in temperature (25°–300°C), pH (0–12), redox state ($\log f_{\text{O}_2(\text{gas})} = -60$ to -20), chloride activity ($\log a_{\text{Cl}^-} = -3$ to $+1$), sulfur activity ($\log a_{\text{dissolved sulfur species}} = -4$ to -1) and activity of carbon species ($\log f_{\text{CO}_2(\text{gas})} = -10$ to $+3$). As part of our study we assessed the quality of the thermodynamic data for zinc aqueous species and minerals. The aqueous speciation of zinc and other relevant species, solubilities of zinc minerals and simulations of physicochemical processes were calculated and depicted using Geochemist's Workbench (Bethke, 1996), a customized version of EQBRM (Anderson and Crerar, 1993), and the Matlab programming environment (Borse, 1997). In most cases we used the thermodynamic properties in the database distributed by the Lawrence Livermore National Laboratory (version 8, revision 6) as contained in Geochemist's Workbench, except where noted below. Activity coefficients for charged aqueous species were estimated using the b-dot version of the extended Debye-Hückel equation (Helgeson, 1969) as included in version 3.2 of Geochemist's Workbench and were assumed to be 1 for neutral aqueous species, except for nonpolar species such as O_{2(aqueous)}, SiO_{2(aqueous)}, CO_{2(aqueous)} and CH_{4(aqueous)}. For calculations at true ionic strengths greater than 3, the ionic strength was assumed to remain constant at that value (see Bethke, 1996, p. 109–114).

Assessment of thermodynamic properties of zinc species

We assessed the reliability of the thermodynamic properties (i.e., $\log K$ of reaction) for zinc aqueous and mineral species by reviewing the literature, comparing published $\log K$ values, and comparing calculated zinc mineral solubilities with experimental values. It was beyond the scope of our study to assess the reliability of related species (e.g., sulfur- and carbon-bearing species), although we discuss possible

uncertainties in the properties of relevant species below. Our extensions and modifications of the Lawrence Livermore National Laboratory database (version 8, revision 6) are noted in Table 1.

Zinc chloride complexes are likely to be the most important in the chloride-rich hydrothermal brines commonly associated with zinc deposits. The two main experimental studies devoted to the aqueous speciation of Zn in chloride brines at elevated temperature are Ruaya and Seward (1986) and Bourcier and Barnes (1987), although Wesolowski et al. (1998) reported experimental data at 200°C. Ruaya and Seward (1986) measured the solubility of $\text{AgCl}_{(\text{solid})}$ in NaCl-ZnCl_2 solutions (0.3–3.5 m total Cl^-) between 100° and 350°C and derived the thermodynamic properties of Zn chloride

complexes present under those conditions. Figure 1a shows that the agreement between the model used in the present paper and the experiments is good at 100°C, especially at low chloride concentration. At 275°C, the predicted silver solubility is approximately four times as high as was measured, despite the fact that the association constants for Zn chloride complexes used in our calculations are those derived by Ruaya and Seward (1986). This discrepancy arises from the different thermodynamic properties for non-Zn species (e.g., $\text{AgCl}_{(\text{solid})}$, Ag^+ , Ag chlorocomplexes, $\text{HCl}_{(\text{aqueous})}$) used by Ruaya and Seward (1986) and in the Lawrence Livermore National Laboratory database, as well as the different activity models used by Ruaya and Seward (1986) and Geochemist's Workbench. We chose not to adjust the properties of the

TABLE 1. Sources of Thermodynamic Data for Zinc Aqueous Species and Minerals Included in the Calculations

Compound	Status	Sources and modifications
Aqueous species		
$\text{Zn(OH)(HS)}_{(\text{aqueous})}$	1	Bourcier and Barnes (1987) extrapolated below 100°C assuming log K versus temperature similar to the other bisulfide complexes of Zn and Pb; $\text{Zn(OH)(HS)}_{(\text{aqueous})} + \text{H}^+ = \text{HS}^- + \text{Zn}^{2+} + \text{H}_2\text{O}$; Log K = -6.0 (25°C), -5.0 (60°C)
$\text{Zn(HS)}_{2(\text{aqueous})}$	1	Bourcier and Barnes (1987); Log K values for $\text{Pb(HS)}_{2(\text{aqueous})}$ from Sverjensky et al. (1997) are used below 100°C because log K versus temperature is similar for Zn and Pb bisulfide complexes, and both complexes have similar values for log K; $\text{Zn(HS)}_{2(\text{aqueous})} = \text{Zn}^{2+} + 2\text{HS}^-$; Log K = -14.71 (25°C), -13.64 (60°C)
Zn(HS)_3^-	1	Bourcier and Barnes (1987); Log K values for Pb(HS)_3^- from Sverjensky et al. (1997) are used below 100°C because log K versus temperature is similar for Zn and Pb bisulfide complexes, and both complexes have similar values for log K; $\text{Zn(HS)}_3^- = \text{Zn}^{2+} + 3\text{HS}^-$; Log K = -16.01 (25°C), -14.82 (60°C)
Zn(HS)_4^{2-}	suppressed	Bourcier and Barnes (1987); this species has been omitted from the model, as it is a minor species even for HS^- concentrations of 1 molal
ZnCl^+	2	Ruaya and Seward (1986)
$\text{ZnCl}_{2(\text{aqueous})}$	2	Ruaya and Seward (1986)
ZnCl_3^-	2	Ruaya and Seward (1986)
ZnCl_4^{2-}	2	Ruaya and Seward (1986)
$\text{ZnCO}_{3(\text{aqueous})}$	2	Zachara et al. (1989) at 25°C; extended to higher temperature by comparison with $\text{CaCO}_{3(\text{aqueous})}$ from Johnson et al. (1992); $\text{ZnCO}_{3(\text{aqueous})} + \text{H}^+ = \text{HCO}_3^- + \text{Zn}^{2+}$; Log K = 5.94 (60°C), 5.40 (100°C), 4.92 (150°C), 4.49 (200°C), 4.01 (250°C), 3.40 (300°C)
ZnHCO_3^+	3	Bourcier and Barnes (1987)
Zn(OH)^+	2	Shock et al. (1997)
$\text{Zn(OH)}_{2(\text{aqueous})}$	2	Shock et al. (1997)
Zn(OH)_3^-	2	Shock et al. (1997)
Zn(OH)_4^{2-}	2	Shock et al. (1997)
$\text{ZnSO}_{4(\text{aqueous})}$	4	Wagman et al. (1982) extrapolated above 200°C assuming log K versus temperature similar to $\text{CaSO}_{4(\text{aqueous})}$ (Sverjensky et al., 1997) and $\text{MgSO}_{4(\text{aqueous})}$ (Shock et al., 1997; from the slop98.dat computer file) and $\text{PdSO}_{4(\text{aqueous})}$ (Sassani and Shock, 1998); $\text{ZnSO}_{4(\text{aqueous})} = \text{SO}_4^{2-} + \text{Zn}^{2+}$; Log K = -5.3 (250°C), -6.3 (300°C)
$\text{H}_2\text{S}_{(\text{aqueous})}$	2	Suleimenov and Seward (1997)
Minerals		
Ferrite-Zn (ZnFe_2O_4)	3	Wagman et al. (1982)
Hydrozincite ($\text{Zn}_5[\text{CO}_3]_2[\text{OH}]_6$)	2	Preis and Gamsjager (2001)
Smithsonite (ZnCO_3)	2	Preis et al. (2000)
Sphalerite (ZnS)	3	Helgeson et al. (1978)
Willemite (Zn_2SiO_4)	2	Free energy and enthalpy of formation from the elements; entropy and volume at 25°C from Robie et al. (1979); heat capacity function from Kubaschewski and Alcock (1979); willemite + $4\text{H}^+ = 2\text{Zn}^{2+} + \text{SiO}_{2(\text{aqueous})}$; Log K = 13.91 (25°C), 11.637(60°C), 9.509(100°C), 7.406 (150°C), 5.725 (200°C), 4.301 (250°C), 2.995 (300°C)
Wurtzite (ZnS)	3	Cox et al. (1989)
Zincite (ZnO)	3	Helgeson et al. (1978)

Values of equilibrium constants extrapolated in this study are listed

Modifications to the Lawrence Livermore National Laboratory (Version 8, Revision 6) thermodynamic database implemented in GWB

1 = Not present in Lawrence-Livermore National Laboratory V8 R6 database

2 = Present in the Lawrence-Livermore National Laboratory V8 R6 database, but replaced by own values

3 = Lawrence-Livermore National Laboratory V8 R6 database (unaltered)

4 = Data for limited temperature range in LLNL V8 R6 database

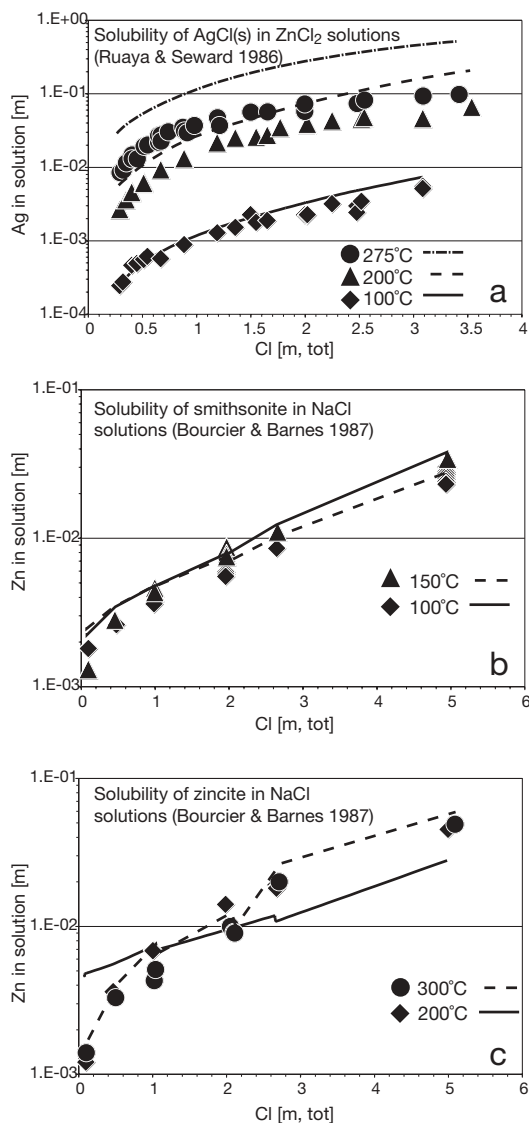


Fig. 1. Comparison of predicted (lines) and measured (symbols) mineral solubilities in chloride solutions. Predictions in this and subsequent figures were calculated using Geochemist's Workbench (Bethke, 1996) using thermodynamic properties reported in the studies listed in Table 1. Activity coefficients of aqueous species were estimated using the b-dot equation of Helgeson (1969) for charged species and assumed equal to 1 for neutral species (see text).

relevant silver and zinc aqueous and mineral species because we do not know which properties are in error and, more importantly, we found that the conclusions drawn from our calculations are not affected. The slope of the predicted solubility curve is similar to that of the experiments and the difference is less than one order of magnitude (Fig. 1a), even at high salinity. Although the discrepancy may be important in reactive or mass transport calculations, it does not affect the calculated change in mineral solubility with salinity or the predicted mineral precipitation sequences. Bourcier and Barnes (1987) measured the solubilities of three zinc minerals, sphalerite in Na-HS solutions and smithsonite and zincite in NaCl-CO₂ solutions. In the latter experiments they measured

the total dissolved zinc concentration and the partial pressure of CO_{2(gas)}, and they used the latter value to calculate the high temperature pH. The predicted zinc concentrations in this study and the measured values for the smithsonite solubility experiments are in excellent agreement (Fig. 1b), in part because of new properties for smithsonite derived by Preis et al. (2000). In the case of zincite solubility, the predicted and measured concentrations are in excellent agreement at 300°C, and within a factor of 3 at 200°C (Fig. 1c).

Other zinc aqueous complexes may be important in some hydrothermal waters and brines (e.g., Zn hydroxide, Zn sulfate, Zn carbonate, Zn acetate, Zn ammine), and a number of those have been included in our calculations (see Table 1). Zn bisulfide complexes are responsible for the transport of significant quantities of zinc only in high sulfur systems in which bisulfide concentrations exceed 0.1 molal. At lower bisulfide concentration, the solubility of sphalerite is so low that Zn bisulfide complexes are unlikely to be important in transporting zinc. Zinc hydroxide complexes have been studied recently by Benzeeth et al. (1999), using measurements of zincite solubility at pH between 4 and 11 and temperature between 75° and 200°C, but their derived thermodynamic properties disagree with those of Hanzawa et al. (1997) and Shock et al. (1997). We chose to retain the values suggested by Shock et al. (1997) because the discrepancies between the three studies are in different directions for each of the zinc species, and in most of our calculations zinc hydroxide complexes were predicted to be insignificant relative to chloride complexes, regardless of which published values we used for the hydroxide complexes.

The log K values of solubility reactions for the minerals sphalerite, wurtzite, zincite, and ferrite Zn were taken from the Lawrence Livermore National Laboratory database, but the values for hydrozincite, smithsonite, and willemite were modified to take into account recent studies (Table 1). Note that we cannot assess the reliability of the properties describing willemite solubility because no experimental data are available. Also, we could not include hemimorphite [Zn₄Si₂O₇(OH)₂ · H₂O] and sauconite [Na_{0.3}Zn₃(Si,Al)₄O₁₀(OH)₂ · 4H₂O], two other important nonsulfide Zn ores, in our calculations owing to the lack of data on their thermodynamic properties.

Speciation of zinc in hydrothermal waters and brines

The speciation of zinc in solution and the stability fields of zinc minerals are shown in a series of activity-activity diagrams (Figs. 2, 3, 4, and 5). Note that in these diagrams we use activities instead of concentrations (i.e., pH, log $f_{O_2(gas)}$, log $f_{CO_2(gas)}$, log a_{Cl^-} , log a_{quartz}) to show the relative effects of changing different physicochemical variables. The effects of each variable are summarized below.

Redox: The most direct effect of redox is the speciation of sulfur, i.e., sulfide or sulfate species (Figs. 2 and 3), which indirectly affects the stability of zinc minerals and zinc speciation. Willemite is stable under oxidizing conditions and high pH (Fig. 2). With increasing temperature, the boundaries between willemite and sphalerite are predicted to shift to more reducing conditions relative to sulfide or sulfate (Fig. 2). At 100°C, willemite + magnetite is predicted to be stable in a small field, but with increasing temperature that field grows. This fact is important in understanding the redox conditions

of willemite formation in hydrothermal environments, and the iron oxide minerals may be useful as indicator minerals in mineral exploration. Under oxidizing conditions, where sulfate predominates over sulfide, the zinc sulfate complex predominates over zinc chlorides at high sulfate activities (Fig. 3a, b). We calculated that the zinc sulfate complex predominates at $a\text{SO}_4^{2-} > 10^{-3}$ at 100°C and either lower or higher values at 300°C, depending on pH (10^{-5} at pH = 3 and 10^{-1} at pH = 7) because of the presence ZnOH^+ . Under reducing conditions, where sulfide species predominate, zinc sulfide complexes can predominate (Fig. 3c, d); however, the solubility of sphalerite is low at pH >3 and dissolved sulfide concentrations (<0.1 molal) encountered in most geologic environments and it is unlikely that much zinc can be transported under such conditions. In both cases where sulfur complexes predominate, the solubility of zinc minerals will increase with increasing concentrations of dissolved sulfur.

pH: In the absence of ligand concentrations high enough to complex the zinc ion, Zn^{2+} predominates under acidic conditions (pH <5–6 at 100°C; pH <2–4 at 300°C) and zinc hydroxide complexes predominate at neutral to basic conditions. Therefore, the solubility of zinc minerals will increase with decreasing pH under acidic conditions and with increasing pH under neutral to basic conditions. Depending on the ligand concentrations a variety of zinc complexes can exist, such as zinc bisulfide, sulfate and/or chloride complexes (Fig. 3). Under the conditions shown in Figure 3, zinc chloride complexes predominate at low pH and higher chloride concentrations and control the solubility of the willemite and sphalerite, whereas at high pH, hydroxide complexes are important. The solubility of zinc minerals shows a minimum at intermediate pH, where zinc sulfide-sulfate complexes predominate depending on the oxidation potential and total concentrations of sulfur.

Temperature: Zinc speciation changes with increasing temperature; e.g., $\text{ZnCl}_{2(\text{aqueous})}$ predominates at 25°C, whereas ZnCl_4^{2-} predominates at 100° to 300°C at the same chloride activity ($a\text{Cl}^- = 1$; Fig. 4). The solubility of zinc minerals is therefore more sensitive to changes in chloride concentration at higher temperature. Figure 3 shows some of the changes in speciation for Zn chloride, sulfide and sulfate complexes at temperatures of 100° and 300°C.

Presence of ligands (Cl^- , HS^- , SO_4^{2-} , OH^- , $\text{CO}_3^{2-}/\text{HCO}_3^-$): The solubility of zinc minerals and the transport of zinc are enhanced by the formation of stable complexes with a number of different ligands in addition to water. The most common ligand in geologic fluids is the chloride ion, and Figure 3 depicts the competition between the chloride ions and the ligands HS^- , SO_4^{2-} , and OH^- . Diagrams are drawn for two different ranges of oxidation potential, i.e., where sulfate species predominate (oxidized; Fig. 3a, c) and where sulfide species predominate (reduced; Fig. 3b, d).

The chloride concentration of the fluid forming Zn deposits varies, but in general lies in the range of 1 molal (approximately 5 wt % NaCl) to greater than 6 molal (approximately 30 wt % NaCl), the highest value reported for many Mississippi Valley-type deposits. Under these conditions, a high-order Zn^{2+} chloride complex, ZnCl_4^{2-} , is predicted to be the main complex responsible for Zn transport in geologic brines at low pH. Zn^{2+} also forms strong complexes with the hydrox-

ide ion, but only under basic conditions (e.g., pH >6, depending on temperature and presence of zinc sulfide and sulfate complexes; Fig. 3; cf. Hanor, 1996).

The solubility of zinc minerals may also increase in the presence of the sulfate ion, especially at low temperature, e.g., <100°C. Figure 3 shows that in sulfate-rich brines (>0.1 molal SO_4^{2-}), the complex $\text{ZnSO}_{4(\text{aqueous})}$ is predicted to be the main dissolved zinc species in neutral to acidic brines. The addition of reduced sulfur causes the precipitation of sphalerite. Therefore, the bisulfide complexes (e.g., $\text{Zn}[\text{OH}][\text{HS}]_{(\text{aqueous})}$ and $\text{Zn}[\text{HS}]_3^-$) are probably not important for the transport of zinc, because the amount of zinc in solution is low (<1 ppm) under these conditions (Hanor, 1996).

The available thermodynamic properties of zinc carbonate and zinc bicarbonate complexes suggest that these species do not play a major role in Zn transport in ore-forming fluids, except possibly the zinc bicarbonate complex at low chloride concentrations (Bourcier and Barnes, 1987).

Fugacity of $\text{CO}_{2(\text{gas})}$ and presence of silica: The fugacity of $\text{CO}_{2(\text{gas})}$ and the amount of dissolved silica affect the relative stabilities of hydrozincite ($\text{Zn}_5[\text{CO}_3]_{12}[\text{OH}]_6$), smithsonite (ZnCO_3), willemite, and zincite (ZnO). Figures 4 and 5 illustrate these relationships as well as the effect of temperature, as a function of pH and $\log f_{\text{CO}_2(\text{gas})}$ (Fig. 4) and $\log a_{\text{quartz}}$ and $\log f_{\text{CO}_2(\text{gas})}$ (Fig. 5). We chose to use the activity of quartz instead of the more common aqueous silica species, $\text{H}_4\text{SiO}_{4(\text{aqueous})}$ or $\text{SiO}_{2(\text{aqueous})}$, to show the degree of quartz undersaturation directly. In order to represent the possibility of amorphous silica controlling dissolved silica, we calculated the diagram for $\log a_{\text{quartz}}$ up to 1.

The stability field of smithsonite shrinks as temperature increases: for example at 25°C, it is stable with respect to willemite at $\log f_{\text{CO}_2(\text{gas})} > -1.6$ (Fig. 4), whereas at 100°C, smithsonite is stable at higher $\log f_{\text{CO}_2(\text{gas})}$ (>0.5). At 300°C, according to our calculations, smithsonite is stable relative to willemite at $\log f_{\text{CO}_2(\text{gas})} > 3$, e.g., approximately 1 kbar partial pressure of $\text{CO}_{2(\text{gas})}$. This calculation is consistent with the common occurrence of smithsonite as a low-temperature alteration product of sphalerite, and we do not expect smithsonite to form readily as a primary mineral in hydrothermal deposits (at least those above approximately 100°C). Note that the diagrams in Figure 4 are drawn for quartz-saturated conditions.

At 25°C hydrozincite is stable at lower $\log f_{\text{CO}_2(\text{gas})}$ than smithsonite and under quartz undersaturated conditions (e.g., >2.5 log units undersaturated; Fig. 5a, b). Hydrozincite is stable at atmospheric $\text{CO}_{2(\text{gas})}$ ($\log f_{\text{CO}_2(\text{gas})} = -3.5$), and its stability field expands as pH increases from 6 to 8 (Fig. 5a, b). The predicted stability of hydrozincite at neutral to basic pH at atmospheric $f_{\text{CO}_2(\text{gas})}$ (Fig. 5b) explains why it is commonly observed as an alteration product of sphalerite not only in the supergene environment but also as a recent product developing in mine dumps. As temperature increases to 100°C, the stability fields of hydrozincite and smithsonite shift to higher $\log f_{\text{CO}_2(\text{gas})}$ and the hydrozincite field shrinks (Fig. 5b, c).

Willemite is stable with respect to zincite at conditions where quartz is less than three orders of magnitude undersaturated ($\log a_{\text{quartz}} > -3$ at 25°C and -3.5 at 100°C; Fig. 5). At higher $\log f_{\text{CO}_2(\text{gas})}$, willemite is stable with respect to hydrozincite only at higher degrees of quartz saturation (Fig. 5).

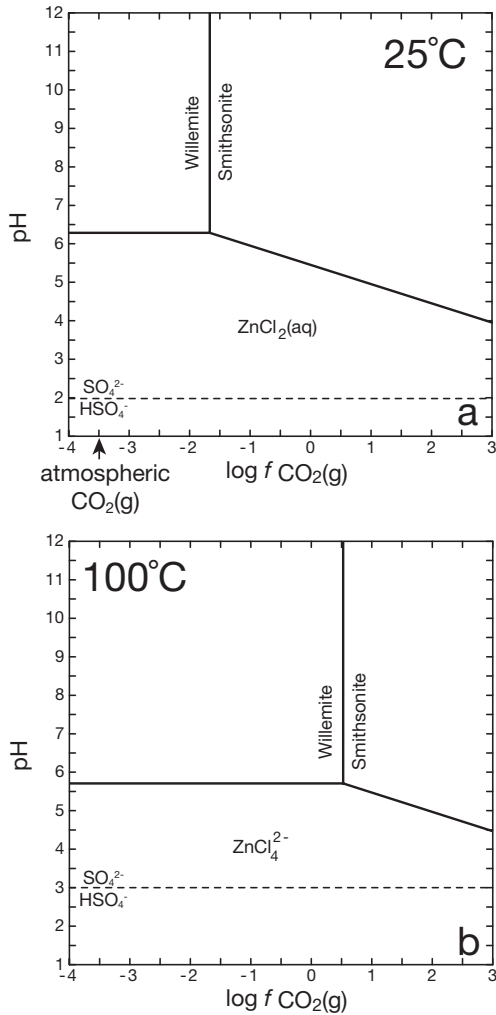


FIG. 4. The effect of pH and fugacity of $\text{CO}_2(\text{gas})$ on the relative stability of willemite and smithsonite at 25°C (a) and 100°C (b). Both diagrams are drawn assuming quartz saturation, activity of Zn species = 0.001 and $a_{\text{Cl}^-} = 1$.

Solubilities of willemite, sphalerite, hydrozincite, smithsonite, and zincite

We calculated the solubility of hydrozincite, smithsonite, sphalerite, willemite, and zincite for a wide range of conditions, systematically varying temperature (50°–300°C), pH (2–8), chloride concentration (0.1–5 m), total sulfur concentration (10^{-4} –0.2 m), dissolved carbon (controlled by the composition of the vapor phase: $\log (f_{\text{CO}_2(\text{gas})} + f_{\text{CH}_4(\text{gas})})$ from –3.5 to 3) and redox conditions (calculated relative to $10^2 < f_{\text{CO}_2}/f_{\text{CH}_4} < 10^{25}$). The solubilities of each of the five minerals were calculated for 73,500 solution compositions. Na concentrations were adjusted to ensure charge balance. The result of these calculations is a matrix of solubilities for each of the five minerals. Some three-dimensional projections from this dataset are presented in Figures 6 and 7. In these diagrams, the solubility of the zinc minerals is expressed as $\log \text{ppm Zn}_{\text{total}}$. The different surfaces are labeled on each graph; one of the surfaces in each graph is semitransparent to make it easier to see the relationships. Note that when one assumes equilibrium,

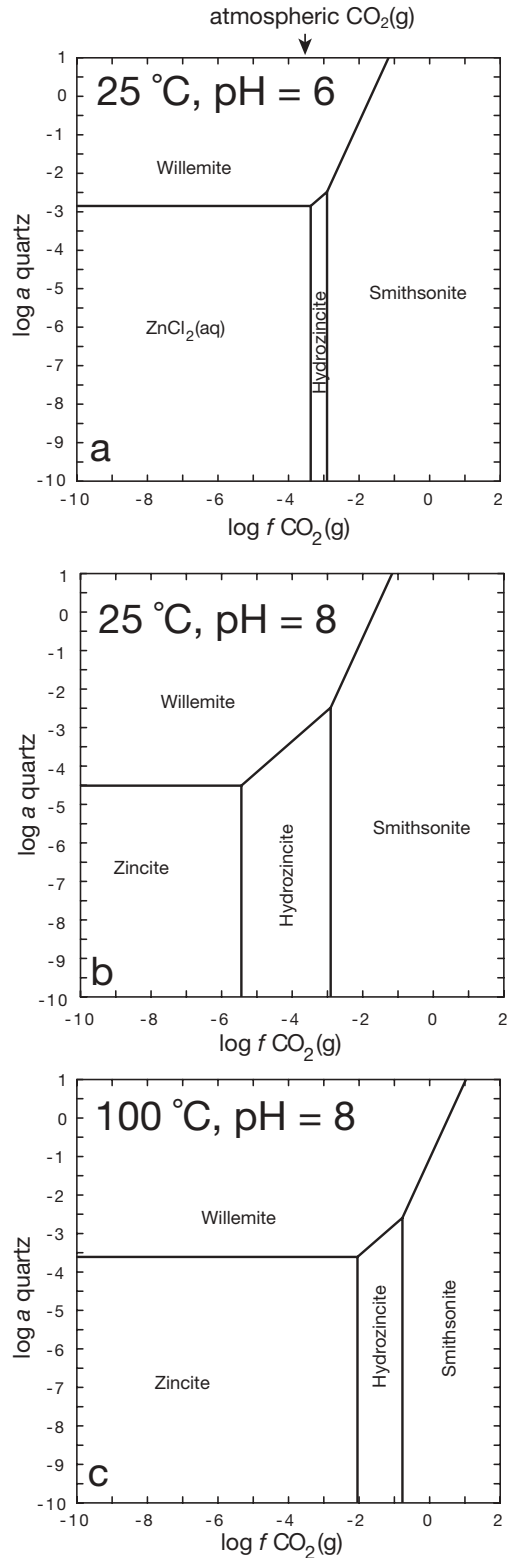


FIG. 5. The effect of the degree of quartz undersaturation (used instead of silica activity to show directly the proximity to quartz), fugacity of $\text{CO}_2(\text{gas})$, and pH on the relative stability of willemite, smithsonite, hydrozincite, and zincite at 25°C (a, b) and 100°C (c). The diagrams are drawn for oxidizing conditions, assuming that carbon is present only as carbonate and sulfur is present only as sulfate. Both diagrams are drawn assuming $a_{\text{Cl}^-} = 1$, activity of sulfate species = 10^{-4} , and activity of Zn species = 0.1.

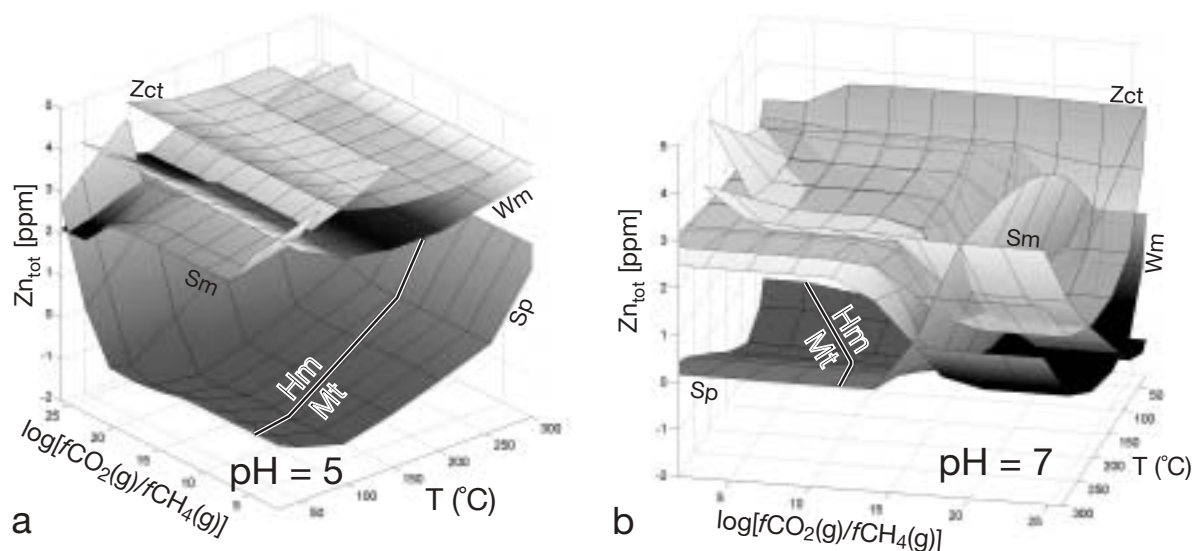


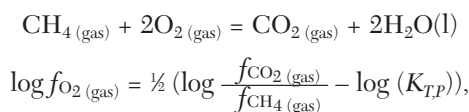
FIG. 6. Predicted solubilities of willemite, sphalerite, zincite, and smithsonite as a function of temperature and redox conditions. Geochemist's Workbench (Bethke, 1996) and Matlab (Borse, 1997) were used to calculate and plot diagrams. Both diagrams are drawn for $(f_{\text{CO}_2} + f_{\text{CH}_4}) = 10$, $\text{Cl}_{\text{tot}} = 1 \text{ m}$, $\text{S}_{\text{total}} = 1 \text{ m}$ and quartz saturation. Hm = hematite, Mt = magnetite, Sm = smithsonite, Sp = sphalerite, Wm = willemite, Zct = zincite.

the mineral controlling Zn concentration in the solution is the one with the lowest solubility, and this mineral is the one that is predicted to precipitate from a supersaturated solution. All the other surfaces are metastable. Some points or parts of the surface may be missing in some diagrams, indicating that the speciation calculation did not converge for these particular conditions. This lack of convergence generally occurs when the solubility of the phase is high ($>>1,000$ ppm Zn), as a result of numerical problems related to maintaining electrical charge balance in the model solutions.

Solubility plots of this type can be used to depict the relative stability of the different minerals and the effects of combinations of variables on their solubilities. The latter is important for recognizing likely precipitation mechanisms, i.e., conditions under which relatively small changes in one or several chemical or physical variables will result in the precipitation of dissolved Zn. The different diagrams depicted here were chosen to show the potential effects of ore-forming processes such as cooling, fluid-rock interaction, and fluid mixing. Solubility plots have an advantage over activity-activity diagrams in that they show concentrations rather than activities and hence can be used directly to show dissolved element concentrations. These plots also show the differences in the relative solubilities of multiple minerals, indicating the magnitude of changes in chemical conditions that will result in the stabilization of a metastable phase. For example, in Figure 6b, calculated for 300°C and oxidized conditions, the proximity of the willemite and zincite surfaces suggests that a small change in a variable not depicted, such as a small decrease in silica activity, will be sufficient to stabilize zincite relative to willemite.

Temperature vs. $f_{\text{O}_2(\text{gas})}$ (e.g., cooling): The diagrams in Figure 6 depict the solubilities of sphalerite, willemite, smithsonite, and zincite as a function of temperature and redox

state at acidic pH (5) and neutral to basic pH (neutral $\text{pH}_{25^\circ\text{C}} = 7$; $\text{pH}_{50^\circ\text{C}} = 6.6$; $\text{pH}_{300^\circ\text{C}} = 5.7$) for a given fugacity of $\text{CO}_2(\text{gas})$ and total concentrations of Cl and S. For reference, a dark line on the sphalerite solubility surface shows the location of the hematite-magnetite boundary as a function of temperature and redox state. The redox scale in Figure 6 is in $\log(f_{\text{CO}_2(\text{gas})}/f_{\text{CH}_4(\text{gas})})$ units, because the redox scale changes with temperature. The $\log(f_{\text{CO}_2(\text{gas})}/f_{\text{CH}_4(\text{gas})})$ scale is related to $\log f_{\text{O}_2(\text{gas})}$ by the following chemical reaction and equation:



where $K_{T,P}$ is the equilibrium constant for the reaction at a given pressure and temperature.

The solubility of sphalerite is low ($[\text{Zn}] < 1$ ppm) at low temperature under reducing conditions, but it increases with increasing temperature above 100°C and also under oxidizing conditions as sulfate replaces sulfide as the predominant sulfur species. The solubility of willemite depends much less on temperature (Fig. 6). Under acidic conditions, the predicted solubility of willemite displays a minimum between 150°C and 200°C but remains extremely high ($>1,000$ ppm; Fig. 6a). Under neutral to basic conditions, the solubility of willemite decreases by about two orders of magnitude as the fluid becomes more oxidized (Fig. 6b). This decrease reflects that the $\text{Zn}(\text{HS})(\text{OH})_{(\text{aqueous})}$ aqueous complex becomes less stable as conditions become more oxidizing and Zn chloride complexes predominate. Under even more oxidizing conditions at basic pH at 300°C , sphalerite dissolves and is replaced by willemite near the hematite-magnetite boundary (Fig. 6b). Under acidic conditions, willemite will crystallize instead of sphalerite only

in the absence of bisulfide in the solution, i.e., under low total sulfur and/or oxidizing (sulfate predominant) conditions, such as near-surface environments. Smithsonite and zincite have generally higher predicted solubilities than sphalerite and willemite for the conditions of runs 6 and 7. The solubility of smithsonite decreases with decreasing temperature, and it may become the stable zinc mineral at low temperature and under basic and oxidized conditions (Fig. 6b). The solubility of zincite varies in a manner similar to that of willemite; zincite may precipitate instead of willemite if the activity of dissolved silica is low enough (e.g., Fig. 5).

Redox state and pH (e.g., fluid mixing or fluid-rock interaction): Figure 7 shows the effects of changing redox state, pH, chloride concentration, and temperature on the solubilities of several zinc minerals. In general, sphalerite has the lowest solubility, i.e., it predominates throughout most of the conditions

shown in Figure 7; however, with increasing temperature, oxidation, and pH, other minerals can have lower solubilities and may precipitate. Note that the solubility of sphalerite increases with decreasing sulfur, i.e., at sulfur concentrations less than the value of 0.01 m used to calculate Figure 7. At low temperature, e.g., 50°C, the solubility of sphalerite is insensitive to changes in pH and redox state, except under very acidic conditions (pH < 3) and/or oxidizing conditions as shown in Figure 7a. With increasing temperature, e.g., 300°C, sphalerite solubility is also insensitive to pH and redox state but over smaller ranges (Fig. 7c). Sphalerite solubility is more strongly affected by pH and oxidation potential at high chloride concentrations, e.g., 5 m (Fig. 7b, d), and at higher temperature (300°C) the solubility of sphalerite strongly depends on pH at slightly basic to acidic conditions (pH < 7). The insensitivity of sphalerite solubility to pH and

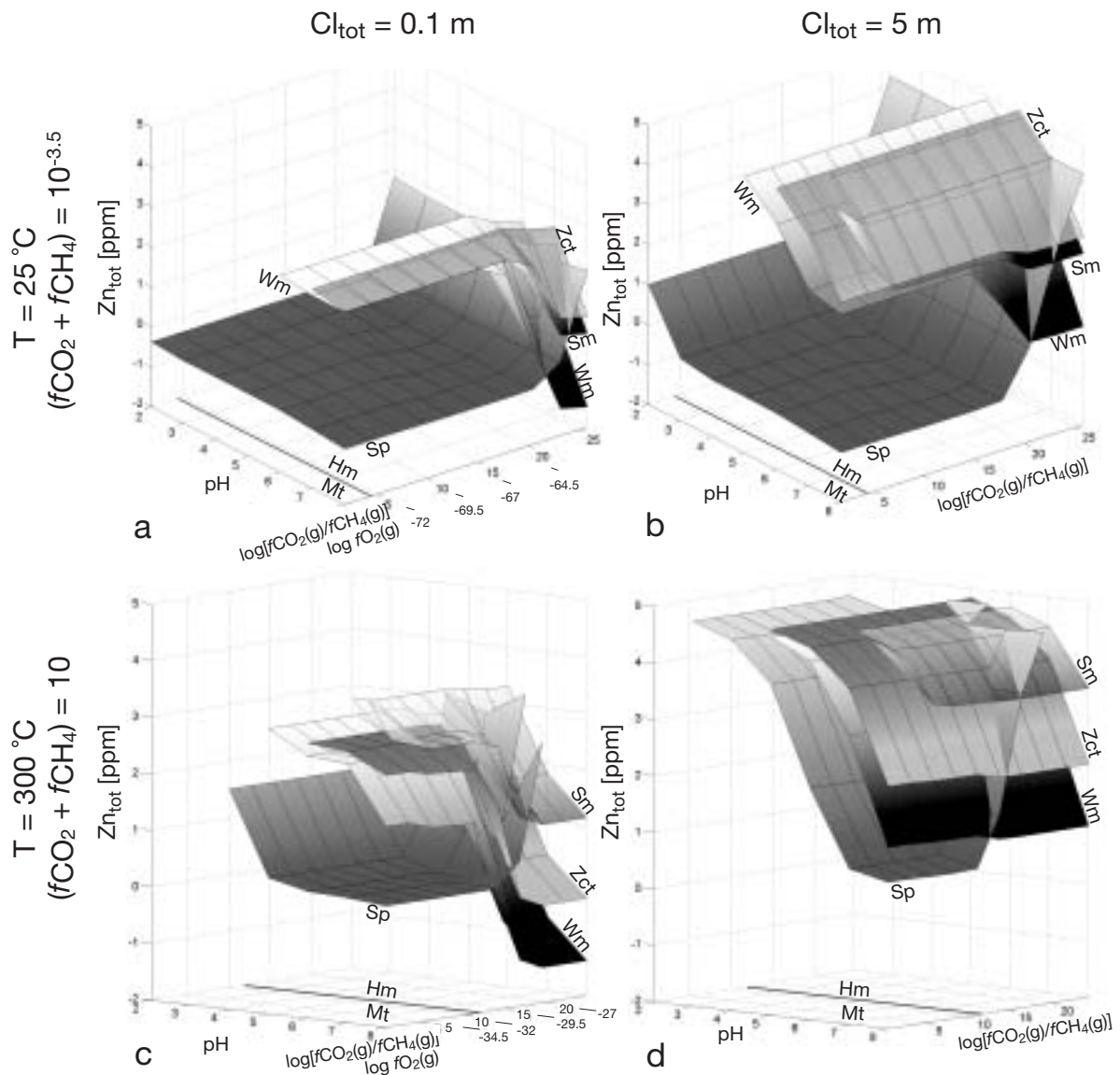
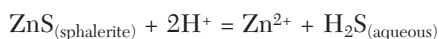
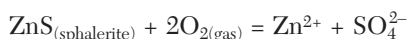


FIG. 7. Solubilities of willemite, sphalerite, zincite, and smithsonite as a function of pH and redox state, temperature, and chlorinity. The diagrams are drawn at quartz saturation, $S_{\text{total}} = 0.01$ m and $(f_{\text{CO}_2} + f_{\text{CH}_4}) = 10^{-3.5}$ at 25°C and 10 at 300°C. Information on calculations and abbreviations as in Figure 6.

oxidation potential at low temperature is due to the following reaction:



which does not involve H^+ or $\text{O}_{2(\text{gas})}$. The effects of oxidation potential and pH at higher temperatures are dominated by the following reactions:



With increasing temperature, the calculated mineral solubility surfaces are closer and they intersect at more reducing conditions and lower pH (Fig. 7). These observations reinforce the results discussed above (i.e., willemite is likely to form instead of sphalerite at $> 200^\circ\text{C}$ and neutral to basic pH > 6 and/or higher oxidation potential; e.g., hematite is stable until temperatures of 300°C , at which magnetite + willemite can be stable). At low temperature, the solubility surfaces for willemite, zincite, and smithsonite are all several orders of magnitude higher than for sphalerite, except at very oxidizing and basic pH conditions. With increasing temperature and chloride concentration, the surfaces for willemite and zincite are much closer to sphalerite, indicating that the silicate and oxide are more likely to precipitate from high temperature brines, even with reduced sulfide present. Smithsonite appears to be most soluble relative to the other zinc minerals at high temperature but is likely to form at low temperature in the absence of reduced sulfide and under quartz-undersaturated conditions, as mentioned above.

Case Study: The Beltana Willemite Deposit

Regional geology

The Beltana willemite deposit is located in the Adelaide geosyncline, a north-south elongated trough that is interpreted to have developed as a rift in the South Australian craton (Fig. 8). The Adelaide geosyncline contains a thick (up to 15 km) Neoproterozoic sedimentary sequence overlain by Lower Cambrian carbonates (Preiss, 1987). The Cambro-Ordovician Delamerian orogeny marked the end of sedimentation. A simplified lithostratigraphic column for the geosyncline is presented in Figure 9. The Beltana deposit is located at the tectonic contact between the diapiric Callanna Group and the Cambrian Ajax Limestone (Figs. 9 and 10). Recent mapping by Perilya Resources resulted in the subdivision of the Ajax Limestone into Woodendinna Dolomite (at the base) that hosts the willemite at Beltana, and lower and upper Wilkavillina Limestones (Groves et al., 2003).

The Callanna Group contains the oldest sediments of the Adelaide geosyncline. The Callanna Group consists of large amounts of mainly basaltic, subaqueous volcanic rocks overlain by thick evaporitic mixed carbonate and clastic sequences, where the evaporites now crop out as numerous diapirs that intrude the younger Neoproterozoic and Lower Cambrian sedimentary rocks (Fig. 8). Diapirism was probably initiated by sediment loading during the Neoproterozoic-Lower Cambrian (Dyson, 2001) and, along with the associated faults,

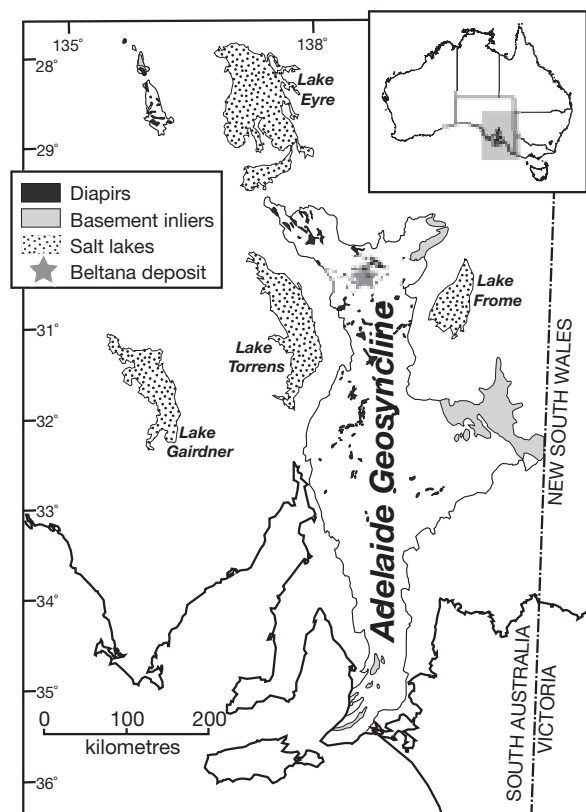


FIG. 8. Location of the Adelaide geosyncline, diapiric occurrences of the Callanna Group, and the Beltana willemite deposit. Modified after Preiss (1987).

reactivated during the Delamerian orogeny. The Callanna Group rocks in the Beltana diapir consist of gray and red shales, commonly containing numerous halite pseudomorphs, and represent sediments that were deposited in hypersaline tidal flats (Preiss, 1987).

The Ajax Limestone is a Lower Cambrian fossiliferous platform carbonate unit, commonly containing abundant archaeocyathids. The least altered Ajax Limestone has a beige color, may be extensively silicified, and consists mainly of calcite. It is commonly dolomitized on a regional scale. This regional dolomite has a brown color in outcrop but is not associated with Fe addition. In the absence of a correlation between brittle structures and this regional dolomitization, it is assumed that dolomitization took place at an early, probably diagenetic stage (Curtis et al., 1991).

Ore mineralogy

At Beltana, willemite occurs in three distinct, steeply dipping saucer-shaped orebodies that pinch out at a maximum depth of approximately 100 m. The host rock is dolomitized Ajax Limestone. The willemite mineralization occurred at the footwall of a major fault that brings a diapiric breccia consisting of Callanna Group rocks in contact with the Ajax Limestone (Fig. 10). In and around the mineralized zone, the Ajax Limestone is colored red by hematitic and dolomitic alteration. Mapping the intensity of the hematitic alteration using a color index scheme shows that hematite alteration follows

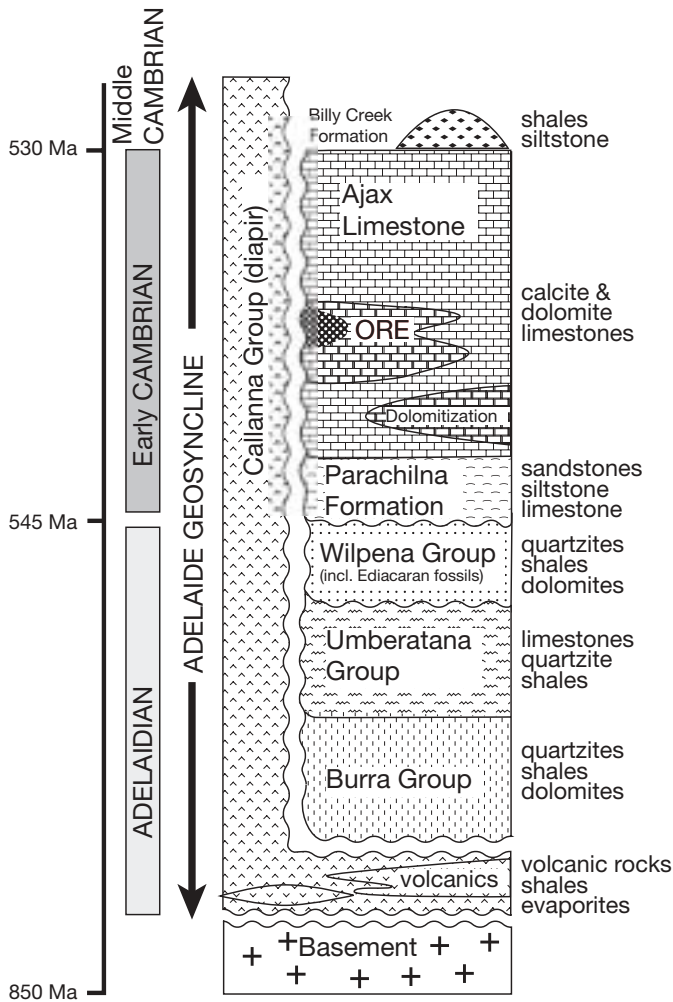


FIG. 9. Simplified stratigraphic column for the Adelaide geosyncline, with location of the Beltana willemite deposit ("ORE" on figure). Modified after Preiss (1987).

the contact between the Beltana diapir and the Ajax Limestone, and that willemite occurs where the hematite alteration is most intense (Burdett, 2000). The contact between the diapir and the Callanna Group is best exposed in the open-cut mine (Fig. 10). On the hanging wall (Callanna Group side), the contact is underlined by white quartzite that may belong to the Callanna Group and that was squeezed along the contact owing to rheologic differences between the quartzite and the embedding shale matrix (arrow L on Fig. 10). On the footwall (Ajax Limestone side), the contact is underlined by a dark band that corresponds to intense hematite alteration (several vol % hematite; arrow D on Fig. 10).

The Beltana deposit contains zinc-rich and lead-rich zones (Horn, 1975; Burdett, 2000; Hallam, 2000). Sulfides are totally absent from the mineralized zone. The ores occur as replacement and as cavity fillings. The main zinc ore is willemite, which occurs predominantly as a white cement lining large cavities. The willemite also occurs as a replacement of dolomitized and hematitized Ajax Limestone. The last mineral to crystallize in the cavities was calcite (or dolomite in some places), and many cavities retain open space. The willemite ore contains high levels of arsenic (0.5 wt % As; Groves et al., 2003). Most of the arsenic and lead (0.4–2.5 wt %) in the willemite ore are hosted in the mineral hedyphane, $\text{Ca}_2\text{Pb}_3(\text{AsO}_4)_3\text{Cl}$, which occurs as a greenish, coarse-crystalline replacement of carbonate or cavity filling and as white, hexagonal, bipyramidal crystals up to 1 cm in cavities (Elliott, 1991). Hedyphane is overgrown by calcite and dolomite in the vugs. Coronadite occurs in the gossan overlying the deposit, in veins and fractures crosscutting the willemite orebody, and as late-stage vug fillings. Coronadite is also the main Pb mineral in the matrix of the karst collapse breccia recognized by Groves et al. (2003). This breccia forms a Pb-rich pipe at the center of the willemite orebody.

Internal sediments in the solution cavities in the willemite ore consist of finely laminated red and white willemite. This bedding is nearly horizontal, whereas the Ajax Limestone



FIG. 10. View toward the south over the Beltana open pit. The arrows labeled L and D point to a quartzite lens (L) and a hematite-rich rock (D) that underline the contact between the Callanna beds and the Ajax Limestone.

beds are steeply dipping, indicating that the willemite mineralization postdated significant deformation (i.e., diapiric intrusion and Delamarian orogeny; Burdett, 2000). Hallam (2000) measured homogenization temperatures from fluid inclusions in hydrothermal calcite that immediately postdates willemite and hedyphane and found temperatures ranging from 70° to 180°C, although most samples had homogenization temperatures between 70° and 130°C. Although Hallam (2000) did not measure many inclusions (46 from six samples), these data help to constrain the mineralization temperatures at Beltana and rule out near-surface low temperature alteration of sulfide ores as an origin for the Beltana willemite. Additional fluid inclusion work reported in Groves et al. (2003) supports this conclusion and demonstrates that saline brines (halite saturation) were involved in the formation of the willemite.

Dynamic modeling of ore transport and deposition at the Beltana willemite deposit

The results from the modeling sections above show that willemite precipitation from hydrothermal solutions is favored by oxidizing conditions (approximately hematite-magnetite and above), neutral to basic pH, and elevated temperatures (>100°C). These conditions are consistent with the geology and mineralogy of the Beltana deposit. First, the mineralization is associated with hematite alteration in the limestone, indicating the involvement of oxidized fluids. The abundance of the arsenate mineral hedyphane associated with willemite also supports the unusually oxidized nature of the mineralizing fluid. Second, the Callanna Group provides a likely source for salinity and metals in the hydrothermal fluid. Although the Callanna group is highly heterogeneous, it contains large volumes of oxidized (hematite-bearing and/or gypsum-anhydrite-bearing) mixed carbonate and clastic sediments that are predominant in the Beltana diapir around and in the mine. The mineralogy of the sediments was determined for three samples from the Beltana open pit using powder X-ray diffraction (Philips PW1800 diffractometer, Co K α radiation, a variable divergence slit and a graphite monochromator, with steps of 0.05° 2 θ with quartz, muscovite (mainly 2M1 polytype, but possibly a mixture with 1M), dolomite, chlorite, microcline, and hematite, and two of the samples may contain small quantities of calcite. Third, the infiltration of hydrothermal fluids from the Callanna Group into the Ajax Limestone is strongly suggested by the distribution of hematite alteration, which is parallel to the fault that controls the diapir, and by the occurrence of a band of intense hematite alteration at the contact between the Callanna Group and the Ajax Limestone (Fig. 10). Fourth, the occurrence of Zn minerals in solution cavities in dolomitic carbonates suggests that an acidic mineralizing fluid reacted with and was buffered by large amounts of carbonate, which would have resulted in the pH of the fluid becoming neutral to slightly basic. Fifth, the fluid inclusion data suggest that the temperature of mineralization may have exceeded 170°C in some places.

In order to test this conceptual model, we simulated fluid mixing and fluid-rock interaction assuming that a hot, acidic fluid derived from the evaporitic clastic Callanna Group reacted with the Ajax Limestone and mixed with the fluids in

the Ajax Limestone. The results of the modeling are shown in Figures 11 and 12. In addition, the model that best represents the paragenetic sequence at Beltana has been used to model the evolution of the stable isotope composition of the Beltana carbonates.

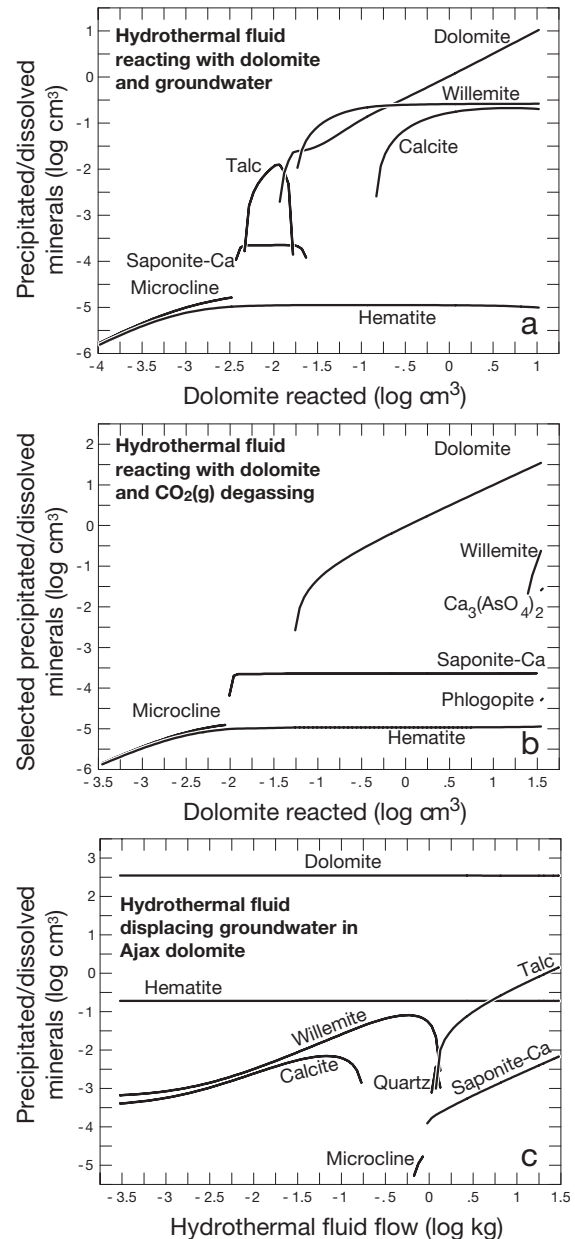


FIG. 11. Predicted sequences of mineral precipitation and dissolution for dynamic geochemical models of the formation of the Beltana deposit. a. Titration of 30 g of dolomite and 300 kg of Ajax limestone groundwater ($T = 120^{\circ}\text{C}$) into 1 kg of hydrothermal fluid ($T = 200^{\circ}\text{C}$). b. Titration of 100 g of dolomite into 1 kg of hydrothermal fluid. $f_{\text{CO}_2(\text{gas})}$ and temperature are assumed to change linearly from 0.3 to 0.01 bars and 200° to 150°C , respectively, during the titration. c. "Flush" model of Geochemist's Workbench (Bethke, 1996): 30 kg of hydrothermal fluid ($T = 200^{\circ}\text{C}$) flow through 1 kg of Ajax limestone, displacing an equivalent amount of Ajax ground water ($T = 120^{\circ}\text{C}$).

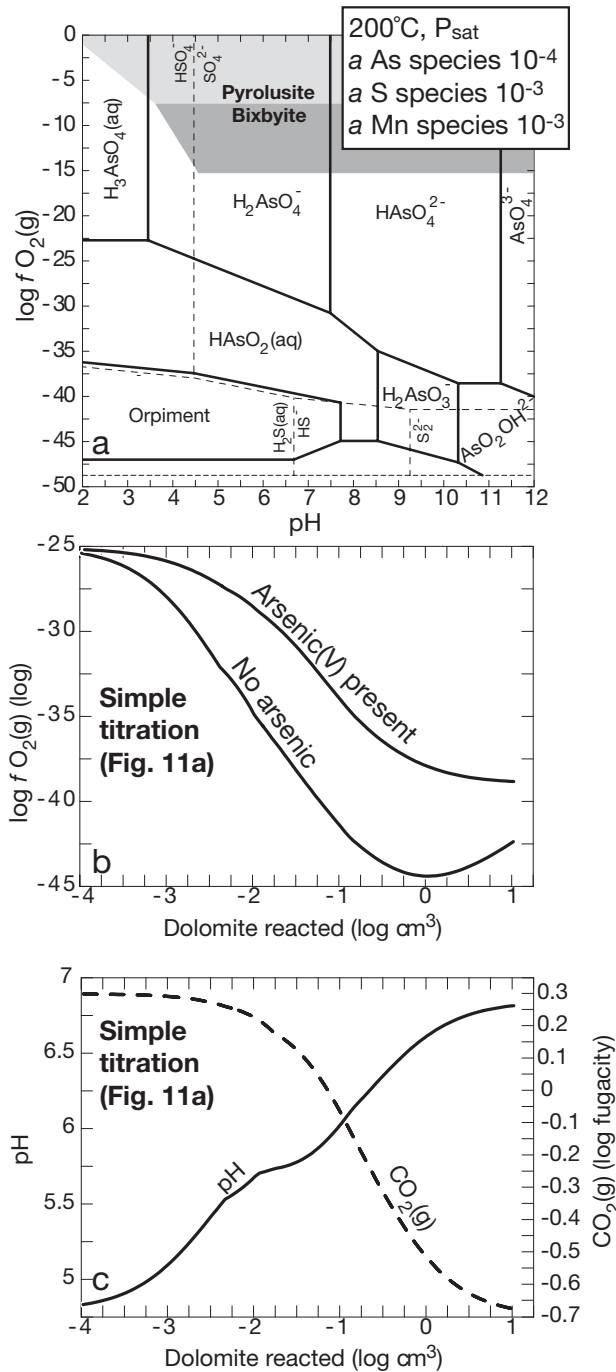


FIG. 12. Effect of arsenic on the evolution of the fluid mixing model of Figure 11a. a. Log $f_{O_2(g)}$ vs. pH diagram illustrating the speciation of As (solid lines) and sulfur (dashed lines) at 300°C. Note that the arsenate-arsenite boundaries are at much more oxidized conditions than the sulfate-sulfide boundaries. b. Evolution of the redox state of the model system in the absence and presence of arsenate species in the hydrothermal fluid. c. Evolution of the pH and $f_{CO_2(g)}$ of the model system.

Simulation of mineral precipitation sequences

In the absence of direct information on the chemistry of the mineralizing fluid or fluids, initial fluid compositions were estimated on the basis of a number of assumptions summarized in Table 2. The ore transporting hydrothermal

fluid was assumed to have been at 200°C, on the basis of the fluid inclusion evidence of 170°C, and in equilibrium with quartz-muscovite-microcline and hematite—the observed mineralogy of the clastic sedimentary rocks in the Callanna Group. Given the strong textural evidence for dolomite dissolution in the Ajax Limestone by the mineralizing fluid, we assumed that the transporting hydrothermal fluid was undersaturated with respect to dolomite ($\log[Q/K] = -3$), even though there are minor amounts of dolomite in the Callanna Group evaporitic sedimentary rocks. We assumed that the fluid is close to saturation with anhydrite ($\log[Q/K] = -0.74$) and is strongly oxidized ($\log f_{O_2(g)} = -25$) because of the ubiquitous presence of hematite and the occurrence of primary arsenate minerals in the orebody. A pH of 4.79 was estimated using the muscovite-quartz-microcline equilibrium and a potassium concentration of 0.41 m (Na/K ratio of 5). The sodium concentration was fixed at 2 molal (approximately three times seawater), and the chloride concentration was adjusted to maintain electrical neutrality ($Cl = 2.45$ molal).

The fluid from the Ajax Limestone is assumed to have been at equilibrium with dolomite and hematite at 120°C, strongly oxidized ($\log f_{O_2(g)} = -10$), and nearly neutral (pH = 6.84), on the basis of an estimated $f_{CO_2(g)}$ of 0.20. The fluid is assumed to have had a low chloride concentration of 0.19 molal.

Figure 11 shows the results of three types of calculations involving the same two end-member fluids (Table 2) but different assumptions for the nature of fluid mixing and fluid-rock interaction (i.e., different ratios of hydrothermal fluid, host rock, and fluid derived from the Ajax Limestone, and different rates of mineral dissolution). Note that owing to the lack of thermodynamic properties, the main Pb ore mineral at Beltana, hedyphane, is not included in the thermodynamic model. The first two models simulate a system initially dominated by a brine transporting the metals. This situation is modeled by titrating dolomite and the water present in the Ajax Limestone into the ore-transporting fluid. In the third model (Fig. 11c), we simulate a rock-dominated system invaded by increasing amounts of hydrothermal fluid.

In the first calculation, we titrated the Ajax Limestone fluid and dolomite into the hydrothermal mineralizing fluid to simulate fluid mixing and concurrent reaction with dolomitic host rock (Fig. 11a). In the second case (Fig. 11b), we assumed only a reaction between the hydrothermal fluid and the dolomite of the Ajax Limestone, in the absence of the water in the Ajax Limestone. In general, dolomite dissolution results in an increase of the partial pressure of $CO_{2(g)}$, which prevents the precipitation of willemite by changing the pH to a slightly acidic condition. Figure 11b depicts the situation where $CO_{2(g)}$ is allowed to escape, which leads to a pH increase toward values that result in willemite precipitation. The results of the third calculation are shown in Figure 11c, where we assumed that the mineralizing hydrothermal fluid displaces an equivalent mass of reacted Ajax fluid (i.e., the “flush” model of Bethke, 1996). In the “flush” model, the initial conditions represent the dolomitized Ajax Limestone (1,000 g of dolomite, 0.12 g of calcite, traces of hematite) and 1 kg of Ajax fluid in equilibrium with the bedrock at 120°C. This calculation simulates the change of composition in the rock as 30 kg of hydrothermal fluid flows through it, gradually displacing an equivalent amount of Ajax fluid.

TABLE 2. Estimated Fluid Compositions for Simulating Ore Formation at the Beltana Willemite Deposit in South Australia

Parameter (unit of measure)	Hydrothermal fluid (assumed saturated with quartz, muscovite, microcline, and hematite)	Ajax Limestone fluid (assumed saturated with dolomite and hematite)
T	200°C	120°C
pH	4.79 (<i>quartz-muscovite-microcline</i>)	6.84 ($f_{\text{CO}_2(\text{gas})}$)
Log $f_{\text{CO}_2(\text{gas})}$	-25.0	-10.0
$f_{\text{CO}_2(\text{gas})}$	2	0.20
Dissolved solids	131 g/kg	13.4 g/kg
Al (ppb)	13 (<i>muscovite saturation</i>)	$9.87 \cdot 10^{-5}$
As (ppm)	69.3	0.005
Ca (ppm)	697	17.8
C (ppm)	201 ($f_{\text{CO}_2(\text{gas})}$)	97.1
Cl (m)	2.45 (<i>charge balance</i>)	0.194 (<i>charge balance</i>)
Fe (ppm)	0.035 (<i>hematite saturation</i>)	$9.5 \cdot 10^{-13}$ (<i>hematite saturation</i>)
Pb (ppm)	8.69	0.099
Mg (ppm)	21.1	0.339 (<i>dolomite saturation</i>)
K (m)	0.41	0.10
Si (ppm)	89.2 (<i>quartz saturation</i>)	4.51
Na (m)	2.00	0.100
S (ppm)	13.9	16.5
Zn (ppm)	174	0.53

Italicized values are calculated assuming mineral saturation, equilibrium with a given $f_{\text{CO}_2(\text{gas})}$, or to insure electrical neutrality of the solution (charge balance), as indicated

The titration calculation (Fig. 11a) reproduces accurately the paragenesis observed at Beltana. The model shows initial dissolution of dolomite (~10 mm³ dolomite/kg of hydrothermal fluid), followed by willemite precipitation and then by calcite precipitation. Willemite precipitation is controlled by the rise in pH to nearly neutral reported in Figure 12c, induced by the change of $f_{\text{CO}_2(\text{gas})}$ from the value in the hydrothermal fluid to the value found in the Ajax fluid. Hematite precipitation started early in the process, contemporaneously with dolomite dissolution, i.e., creation of pore space. Talc is predicted to appear as the system nears equilibrium with dolomite, but it is predicted to redissolve shortly after this equilibrium is achieved. Paragenetically early talc has not yet been described at Beltana, but no systematic study of the clay mineralogy of the deposit exists. Talc is known only in minor quantities as a late-stage products in the vugs.

The calculation in Figure 11b (no Ajax fluid involved) similarly predicts initial dolomite dissolution (porosity creation) concomitant with hematite precipitation. Small quantities of clay minerals (phlogopite, Ca saponite) are also predicted to appear early in the paragenetic sequence. Willemite appears only at the end of the reaction path, accompanied by a calcium arsenate. Calcite is not predicted to appear after willemite in this model.

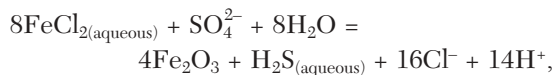
The flush calculation (Fig. 11c) indicates an initial crystallization of willemite and calcite. As reaction progresses, calcite and then willemite redissolve, whereas large quantities of talc start to precipitate. Dolomite and hematite remain stable during the whole reaction path. This precipitation and dissolution sequence is in poor agreement with the observed paragenetic sequence.

In the case of Beltana a simple fluid-mixing model, in the presence of dolomite from the host rock (Fig. 11a), furnishes an accurate representation of the observed paragenetic sequence.

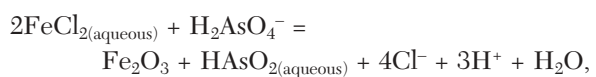
Role of arsenate

Preliminary calculations using a simpler initial fluid composition (i.e., no arsenic) predicted that sulfate reduces to sulfide, resulting in the precipitation of sulfide minerals, something that is not observed at Beltana. Given the presence of hedyphane in the deposit, we incorporated arsenic in our calculations and found that it had a significant effect on the predicted changes in oxidation potential and resulted in the stabilization of willemite rather than sphalerite.

The mineralizing fluid must have carried large quantities of oxidized arsenic (arsenate), as demonstrated by the large amounts of hedyphane observed in the Beltana deposit. Iron in the mineralizing hydrothermal fluid is predicted to occur as an Fe(II) chloride complex, and hence the precipitation of hematite is an oxidation reaction. In the absence of arsenic, hematite precipitation causes the reduction of sulfate to bisulfide, e.g.,



which results in a rapid drop in $\log f_{\text{O}_2(\text{gas})}$ and leads to the precipitation of sulfides (Fig. 12b). In runs with no arsenic present, galena and/or sphalerite are usually predicted to precipitate during the latter part of the reaction path. However, in the presence of dissolved arsenate, the precipitation of hematite will proceed according to



which buffers the redox conditions at values well above the predominance area of reduced sulfur species (i.e., near the boundary between the predominance areas of the arsenate and arsenite species, Fig. 12), with the result that no sulfide

mineral is stable throughout the whole reaction path (Fig. 12b).

Syngenetic or diagenetic arsenates have not yet been found in the Adelaide geosyncline, but their presence would provide a source for the arsenic in the Beltana deposit and would also explain the very oxidized nature of the hydrothermal fluids that are responsible for the formation of this deposit. Exhalative and diagenetic occurrences of arsenates have been reported in other sedimentary sequences (e.g., Bermanec et al., 1993; Brugger and Gieré, 2000), and syngenetic hydrothermal activity has recently been recognized in the Adelaide geosyncline by von der Borch (1999), who interprets chalcidony-cemented dolomitic lenses from the Proterozoic Bunyeroo Formation (Wilpena group, Fig. 9) as hydrothermal mounds (“cold vents”).

Coronadite

Coronadite, one of the main Pb-bearing minerals at Beltana, contains manganese in its tetravalent oxidation state. No thermodynamic data are available for coronadite, but Mn(IV) minerals appear to be stable only under near-surface conditions where free oxygen is available (Fig. 12a). Hypogene coronadite has been described from a number of deposits (see review by Hewett, 1971), but well-documented occurrences of hydrothermal Mn⁴⁺ minerals are scarce, and detailed studies have demonstrated that at least some of the occurrences thought to be hypogene were indeed supergene (e.g., O'Reilly, 1992). Hence, we interpret coronadite as a late product, formed when fresh oxygen-bearing meteoritic fluids penetrated the willemite orebody following the collapse of the hydrothermal karst. This explanation takes into account the thermodynamic and paragenetic evidence, as well as the Ordovician K-Ar age for the Beltana coronadite (Groves et al., 2003). The fact that coronadite is locally overgrown by calcite that contains fluid inclusions with homogenization temperatures in excess of 70°C (C.E. Carman, pers. commun.) indicates that the karst collapse happened as the hydrothermal system was still active.

Simulation of isotopic variation

Burdett (2000) measured the isotope ratios of carbon and oxygen in dolomite and calcite from the Beltana and nearby Aroona willemite deposits. The dolomitized Ajax Limestone defines a clear linear trend on a $\delta^{13}\text{C}$ Pee Dee belemnite (PDB) vs. $\delta^{18}\text{O}$ PDB diagram (Fig. 13). The fresh Ajax dolomite has a composition close to that of Cambrian seawater (Ajax dolomite: $\delta^{13}\text{C} = 0$ and $\delta^{18}\text{O} = -7$; Cambrian seawater: $\delta^{13}\text{C} = 0$, $\delta^{18}\text{O} = -4$). The dolomite samples that have undergone hematite alteration define a linear trend toward more positive $\delta^{13}\text{C}$ and more negative $\delta^{18}\text{O}$, where the most altered samples have $\delta^{13}\text{C}$ of 4 and $\delta^{18}\text{O}$ of -13. Most vug-filling, postwillemite calcite and dolomite have $\delta^{13}\text{C}$ values that cluster between -1 and +2 and $\delta^{18}\text{O}$ values between -22 and -18.

The stable isotope composition of the fluid and minerals during mineralization was modeled using Geochemist's Workbench in the titration run (Figs. 11a and 12). The model takes into account only the temperature dependence of fluid-mineral isotopic fractionation. The fractionation coefficients are from Northrop and Clayton (1966) and Shepard (1984)

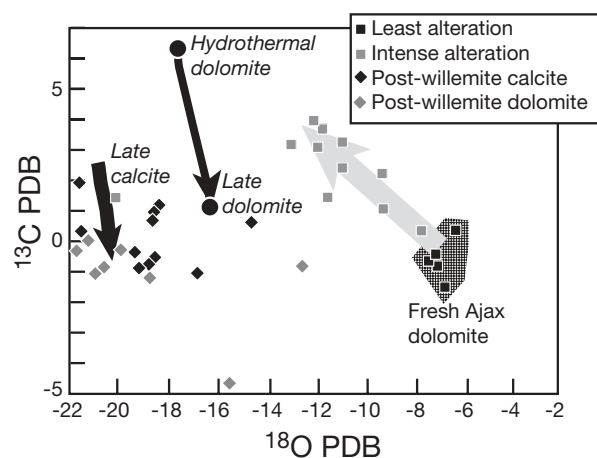


FIG. 13. Oxygen and carbon isotope composition of carbonates from the Beltana and Aroona willemite deposits (Burdett, 2000). Squares represent fresh and altered dolomites from the Ajax limestone, and diamonds represent hydrothermal dolomite and calcite precipitated in cavities. The thick gray arrow emphasizes the trend shown by the Ajax dolomite submitted to increasing degrees of hydrothermal alteration. The italicized labels show the position of the end members compositions calculated using the fluid mixing model of Figure 11a, and the black arrows show the evolution of the calculated mineral composition.

for dolomite, and Bottinga (1969) and O'Neil et al. (1969) for calcite. We assumed that the mineralizing fluid had a starting $\delta^{18}\text{O}$ PDB of -30, similar to present-day seawater, and that the Ajax fluid had a somewhat lighter isotopic composition ($\delta^{18}\text{O}$ PDB = -35). The dissolved carbonate in the hydrothermal fluid has $\delta^{13}\text{C} = 6$, whereas the dolomite and the dissolved carbonate in the Ajax Limestone have $\delta^{13}\text{C} = -0.5$. The model showed initial precipitation of dolomite with $\delta^{13}\text{C} = 6$ and $\delta^{18}\text{O} = -17$. Mixing between this “hydrothermal” dolomite and the Ajax dolomite explains the trend observed with increasing hematitic alteration in the isotopic composition of the Ajax dolomites (large arrow in Fig. 13). The predicted isotopic composition of the late calcite is $\delta^{13}\text{C} = 2.5 - 0.0$ and $\delta^{18}\text{O} = -20.5$ to -21 , and that of the coexisting dolomite is $\delta^{13}\text{C} \approx 1$ and $\delta^{18}\text{O} \approx -16$. This range of values is close to those measured in late-stage carbonates (Fig. 13).

Conclusions

We have used thermodynamic modeling to understand the formation of willemite under hydrothermal conditions. This type of modeling is a powerful tool for predicting physico-chemical conditions under which a particular mineral assemblage is stable and for identifying the geochemical processes that result in the precipitation of ore and other minerals. Our assessment of the thermodynamic properties of aqueous complexes and mineral of Zn shows that the properties for zinc chloride complexes (Ruaya and Seward, 1986), smithsonite (Preis et al., 2000), zincite (Helgeson et al., 1978), and hydrozincite (Preis and Gamsjager, 2000) are reliable; the calculated and measured solubilities are within 0.2 log units, at temperatures up to at least 100°C and in solutions up to 5 molal NaCl. In the case of the solubilities of smithsonite and zincite, agreement between calculated and measured solubilities is within 0.2 log units up to 300°C. We did not assess the

reliability of zinc hydroxide, sulfate, carbonate, or other aqueous complexes of zinc, but in many ore-transporting and ore-forming environments they are likely to be less important than zinc chloride complexes.

Willemite is stable with respect to sphalerite in hydrothermal environments at elevated temperature ($>100^{\circ}\text{C}$), neutral to basic pH, oxidized conditions (at or above the hematite-magnetite buffer), and/or in the absence of dissolved sulfide. Increasing pH is an efficient way to precipitate willemite. Acidic ore-bearing fluids equilibrated with oxidized, clastic rocks will likely precipitate willemite when reacting with carbonate rocks, in particular if the fluids mix with a large volume of carbonate-equilibrated brines. Dynamic geochemical modeling shows that this situation explains the formation of the Beltana willemite deposit. The hydrothermal model also explains in a simple manner the observed carbon and oxygen isotope signature of the carbonates at Beltana. The model also suggests that hematite alteration will be ubiquitous around low to medium ($<250^{\circ}\text{C}$) temperature hydrothermal willemite deposits.

The Adelaide geosyncline provides the general geochemical conditions favorable for hydrothermal willemite formation. It contains large volumes of oxidized clastic rocks capped by carbonate sediments, and its tectonic evolution (diapirism and Delamerian orogen) provided many opportunities for large-scale flow of basinal brines (e.g., Foden et al., 2000). Indeed, additional willemite reserves have been recently discovered near Beltana at Reliance (Groves et al., 2002).

Smithsonite is an abundant mineral at Reliance, where it developed at the expense of willemite during late-stage karstification of the willemite orebody. The thermodynamic modeling shows that, in contrast to willemite, smithsonite is unlikely to precipitate at elevated temperature but is stable in the supergene environment. A similar situation exists for hydrozincite. Hydrothermal smithsonite or hydrozincite deposits are unlikely. This conclusion is consistent with most known occurrences of these minerals, including the new Reliance discovery. Zincite, on the other hand, exhibits a behavior similar to that of willemite, although it has a higher solubility than willemite at quartz saturation. Zincite will precipitate under hydrothermal conditions instead of willemite if quartz is sufficiently undersaturated. This conclusion explains the coexistence of willemite and zincite in deposits such as Franklin, New Jersey.

The numerical modeling at the Beltana deposit also suggests the importance of some trace elements in the formation of sulfide-free willemite deposits. Arsenate in the ore-forming fluid appears to have played a role in preventing the reduction of sulfate to sulfide in response to the oxidation of dissolved ferrous iron to hematite. This situation further illustrates the sensitivity of hydrothermal willemite precipitation to a number of geochemical parameters. Note that in general the role of non-ore trace elements in the formation of ore deposits is poorly understood, and modeling of the type shown here can be used to investigate this question.

In view of the present study, the rarity of hydrothermal willemite deposits is explained by the requirement for a number of geochemical conditions that are rarely met in nature at scales enabling the formation of economic Zn deposits. In

contrast, most sulfide Zn deposits form because of the extremely low solubility of Zn sulfides at low temperature in the presence of dissolved sulfide; the interaction of a metal-rich, sulfide-free fluid with a reducing and/or sulfide-rich rock or fluid triggers quantitative precipitation of Zn sulfides. This situation can occur at a large scale in numerous geologic situations, including many sedimentary sequences where redox boundaries are commonly encountered.

Acknowledgments

We wish to thank Mark Raven (CSIRO Soil & Water, Adelaide) for performing the X-ray diffraction analyses. This project was initiated by a request by PASMINGCO, and we are grateful to David Lawie and Terry Lees for their support and many stimulating discussions. We express special gratitude to Donald F. Sangster for editing this special volume and to Greg Anderson and John Lydon for insightful reviews and many helpful suggestions. This work has been supported by a Swiss National Fund for Scientific Research fellowship (8220-056519) and an Australian Research Council fellowship (DP0208323) to J. Brugger.

REFERENCES

- Anderson, G.M., and Crerar, D.A., 1993, Thermodynamics in geochemistry. Appendix E: New York, Oxford University Press, p. 491–500.
- Bariand, P., Cesbron, F., and Geffroy, J., 1977, Les minéraux, leurs gisements, leurs associations: Meung-sur-Loire, France, Editions Minéraux et Fossiles, (v. 1) and Orleans, France, Bureau de Recherches Géologiques et Minières (v. 2 and 3), 490 p.
- Benezeth, P., Palmer, D.A., and Wesolowski, D.J., 1999, The solubility of zinc oxide in 0.03 m NaTr as a function of temperature, with in situ pH measurement: *Geochimica et Cosmochimica Acta*, v. 63, p. 1571–1586.
- Bermanec, V., Balen, D., Scavnicar, S., and Tibljas, D., 1993, Zn-rich magnetoplumbite from Nezilovo, Macedonia: *European Journal of Mineralogy*, v. 5, p. 957–960.
- Bethke, C.M., 1996, Geochemical reaction modeling, concepts and applications: New York, Oxford University Press, 397 p.
- Borse, G.J., 1997, Numerical methods with MATLAB: Boston, PWS Publishing Company, 584 p.
- Bottinga, Y., 1969, Calculated fractionation factors for carbon and hydrogen isotope exchange in the system calcite-carbon dioxide-graphite-methane-hydrogen-water-vapor: *Geochimica et Cosmochimica Acta*, v. 33, p. 49–64.
- Bourcier, W.L., and Barnes, H.L., 1987, Ore solution chemistry VII. Stabilities of chloride and bisulfide complexes of zinc to 350°C : *ECONOMIC GEOLOGY*, v. 82, p. 1839–1863.
- Brugger, J., and Gieré, R., 2000, Origin and distribution of some trace elements in metamorphosed Fe-Mn deposits, Val Ferrera, eastern Swiss Alps: *Canadian Mineralogist*, v. 38, p. 1093–1119.
- Burdett, M., 2000, Origin of the Beltana and Aroona willemite deposits, Flinders Ranges, South Australia: Unpublished honors thesis, Melbourne, Australia, University of Melbourne, 54 p.
- Cairncross, B., 1997, The Otavi Mountain Land Cu-Pb-Zn-V deposits, Namibia: *The Mineralogical Record*, v. 28, p. 109–131.
- Cox, J.D., Wagman, D.D., and Medvedev, V.A., 1989, Codata key values for thermodynamics: New York, Hemisphere Publications, 271 p.
- Curtis, J.L., Jenkins, G.W., and Gravestock, D.I., 1991, Mississippi Valley-type lead-zinc mineralisation, northern Flinders Ranges, South Australia: Department of Mines and Energy Report Book, v. 91/102, 63 p.
- Dyson, I.A., 2001, The diapir-base metal association in the northern Flinders Ranges: *Mines and Energy South Australia (MESA) Journal*, v. 22, p. 37–43.
- Elliott, P., 1991, Minerals of the Beltana mine: *The Mineralogical Record*, v. 22, p. 449–456.
- Finch, A.A., 1990, Genthelvitite and willemite, zinc minerals associated with alkaline magmatism from the Motzfeldt centre, south Greenland: *Mineralogical Magazine*, v. 54, p. 407–412.
- Foden, J., Barovich, K., Jane, M., and O'Halloran, G., 2000, Sr-isotopic evidence for Late Neoproterozoic rifting in the Adelaide geosyncline at 586

- Ma: Implications for a Cu ore forming fluid flux: *Precambrian Research*, v. 106, p. 291–308.
- FrondeL, C., and Baum, J.L., 1974, Structure and mineralogy of the Franklin zinc-iron-manganese deposit, New Jersey: *ECONOMIC GEOLOGY*, v. 69, p. 157–180.
- Groves, I.M., Gregory, I., and Carman, C., 2002, Reliance—A new high-grade zinc silicate-oxide discovery in the Flinders Ranges: *Mines and Energy South Australia (MESA) Journal*, v. 25, p. 6–10.
- Groves, I.M., Carman, C.E., and Dunlap, W.J., 2003, Geology of the Beltana willemite deposit, Flinders Ranges, South Australia: *ECONOMIC GEOLOGY*, v. 98, p. 797–818.
- Hallam, J., 2000, The geology of the Puttapa willemite deposits, South Australia: Unpublished honors thesis, Melbourne, Australia, University of Melbourne, 65 p.
- Hanor, J.S., 1996, Controls on the solubilization of lead and zinc in basinal brines, in Sangster, D.F., ed., Carbonate-hosted lead-zinc deposits: Society of Economic Geologists Special Publication 4, p. 483–500.
- Hanzawa, Y., Hiroishi, D., Matsuura, C., Ishigure, K., Nagao, M., and Haginuma, M., 1997, Hydrolysis of zinc ion and solubility of zinc oxide in high-temperature aqueous systems: *Nuclear Science and Engineering*, v. 127, p. 292–299.
- Helgeson, H.C., 1969, Thermodynamics of hydrothermal systems at elevated temperatures and pressures: *American Journal of Science*, v. 267, p. 729–804.
- Helgeson, H.C., Delany, J.M., Nesbitt, H.W., and Bird, D.K., 1978, Summary and critique of the thermodynamic properties of rock-forming minerals: *American Journal of Science*, v. 278a, 229 p.
- Hewett, D.F., 1971, Coronadite—Modes of occurrence and origin: *ECONOMIC GEOLOGY*, v. 66, p. 164–177.
- Horn, R.A., 1975, Beltana and Aroona willemite orebodies: The Adelaide geosyncline and Stuart Shelf: Australasian Institute of Mining and Metallurgy (AusIMM) Special Publication, p. 548–553.
- Johnson, C.A., Rye, D.M., and Skinner, B.J., 1990, Petrology and stable isotope geochemistry of the metamorphosed zinc-iron-manganese deposit at Sterling Hill, New Jersey: *ECONOMIC GEOLOGY*, v. 85, p. 1133–1161.
- Johnson, J.W., Oelkers, E.H., and Helgeson, H.C., 1992, SUPCRT92: A software package for calculating the standard molal thermodynamic properties of minerals, gases, aqueous species and reactions from 1 to 5000 bars and 0° to 1000° C: *Computational Geosciences*, v. 18, p. 899–920.
- Kubaschewski, O., and Alcock, C.B., 1979, *Metallurgical thermochemistry—fifth edition*. Oxford, Pergamon Press, 449 p.
- Monteiro, L.V.S., Bettencourt, J.S., Spiro, B., Graça, R., and De Oliveira, T.F., 1999, The Vazante zinc mine, Minas Gerais, Brazil: Constraints on willemitic mineralisation and fluid evolution: *Exploration and Mining Geology*, v. 8, p. 21–42.
- Northrop, D.A., and Clayton, R.N., 1966, Oxygen isotope fractionations in systems containing dolomite: *Journal of Geology*, v. 74, p. 174–196.
- O'Neil, J.R., Clayton, R.N., and Mayeda, T.K., 1969, Oxygen isotope fractionation in divalent metal carbonates: *Journal of Chemical Physics*, v. 51, p. 5547.
- O'Reilly, G.A., 1992, Petrographic and geochemical evidence for a hypogene origin of granite-hosted, vein-type Mn mineralization at the New Ross Mn deposits, Lunenburg County, Nova Scotia, Canada: *ECONOMIC GEOLOGY*, v. 87, p. 1275–1300.
- Piranjo, F., and Joubert, B.D., 1993, An overview of carbonate-hosted deposits in the Otavi Mountain Land, Namibia: Implications for ore genesis: *Journal of African Earth Sciences*, v. 16, p. 265–272.
- Preiss, W.V., 1987, The Adelaide geosyncline—Late Proterozoic stratigraphy, sedimentation, palaeontology and tectonics: Geological Survey of South Australia, Bulletin 53.
- Preis, W., and Gamsjager, H., 2001, (Solid plus solute) phase equilibria in aqueous solution. XIII. Thermodynamic properties of hydrozincite and predominance diagrams for (Zn²⁺ + H₂O + CO₂): *Journal of Chemical Thermodynamics*, v. 33, p. 803–819.
- Preis, W., Konigsberger, E., and Gamsjager, H., 2000, Solid-solute phase equilibria in aqueous solution. XII. Solubility and thermal decomposition of smithsonite: *Journal of Solution Chemistry*, v. 29, p. 605–618.
- Robie, R.A., Hemingway, B.S., and Fisher, J.R., 1979, Thermodynamic properties of minerals and related substances at 298.15 K and 1 bar (10⁵ pascals) pressure and at higher temperatures: U.S. Geological Survey Bulletin, v. 1452, 456 p.
- Ruaya, J.R., and Seward, T.M., 1986, The stability of chlorozinc(II) complexes in hydrothermal solutions up to 350°C: *Geochimica et Cosmochimica Acta*, v. 50, p. 651–661.
- Sassani, D.C., and Shock, E. L., 1998, Solubility and transport of platinum-group elements in supercritical fluids: Summary and estimates of thermodynamic properties for Ru, Rh, Pd, and Pt solids, aqueous ions, and complexes to 1000°C and 5 kbar: *Geochimica et Cosmochimica Acta*, v. 62, p. 2643–2671.
- Sheppard, M.F., 1984, Isotopic geothermometry, in Lagache, M.E., ed., Thermométrie et barométrie géologiques: Société Française de Minéralogie et Cristallographie, p. 349–412.
- Shock, E.L., Sassani, D.C., Willis, M., and Sverjensky, D.A., 1997, Inorganic species in geologic fluids—Correlations among standard molal thermodynamic properties of aqueous ions and hydroxide complexes: *Geochimica et Cosmochimica Acta*, v. 61, p. 907–950.
- Suleimenov, O.M., and Seward, T.M., 1997, A spectrophotometric study of hydrogen sulphide ionisation in aqueous solutions to 350°C: *Geochimica et Cosmochimica Acta*, v. 61, p. 5187–5198.
- Sverjensky, D.A., Shock, E.L., and Helgeson, H.C., 1997, Prediction of the thermodynamic properties of aqueous metal complexes to 1000°C and 5 kb: *Geochimica et Cosmochimica Acta*, v. 61, p. 1359–1412.
- Sweeney, M.A., Pattrick, R.A.D., Vaughan, D.J., and Turner, P., 1991, The nature and genesis of the willemite deposits of Zambia, in Pagel, M., and Leroy, J.L., eds., Source, transport and deposition of metals: Rotterdam, Balkema, p. 139–142.
- Takahashi, T., 1960, Supergene alteration of zinc and lead deposits in limestone: *ECONOMIC GEOLOGY*, v. 55, p. 1083–1115.
- von der Borch, C.C., 1999, Submarine spring mounds and related deposits in the lower Bunyeroo Formation, northern Flinders Ranges: *Mines and Energy South Australia (MESA) Journal*, v. 15, p. 35–39.
- Wagman, D.D., Evans, W.H., Parker, V.B., Schumm, R.H., Halow, I., Bailey, S.M., Churney, K.L., and Nuttall, R.L., 1982, The NBS tables of chemical thermodynamic properties, selected values for inorganic and c1 and c2 organic substances in SI units: *Journal of Physical and Chemical Reference Data*, v. 11, supp. 2, 392 p.
- Wesolowski, D.J., Benezeth, P., and Palmer, D.A., 1998, ZnO solubility and Zn²⁺ complexation by chloride and sulfate in acidic solutions to 290°C with in-situ pH measurement: *Geochimica et Cosmochimica Acta*, v. 62, p. 971–984.
- Zachara, J.M., Kittrick, J.A., Dake, L.S., and Harsh, J.B., 1989, Solubility and surface spectroscopy of zinc precipitates on calcite: *Geochimica et Cosmochimica Acta*, v. 53, p. 9–19.